JTTEE5 2:45-50
©ASM International

Planning Robotic Trajectories for Thermal Spray Shape Deposition

M.M. Fasching, F.B. Prinz, and L.E. Weiss

Thermal spray shape deposition is a new process for fabricating net-shape parts by incremental material buildup of cross-sectional layers. This article presents an approach for spraying thin, flat layers using a robotic thermal spray system. Asymmetries of the spray distribution are first corrected by tilting the spray torch based on a computer model of the measured spray distribution. The path of the torch is then found using heuristics that are based on the estimated standard deviation of the corrected distribution. For example, thick arc-sprayed coatings of approximately 4.0 mm thickness have been deposited using this method, with the resulting standard deviation from the mean thickness ranging from 20.0 to 30.0 μm. To demonstrate the shape deposition process, a prototype turbine blade shape was built using these optimized trajectories.

1. Introduction

A THERMAL spray forming system has been developed at Carnegie Mellon University to fabricate three-dimensional net shapes using a layered deposition process.[1] The basis for this approach, called MD* (to recursively mask and deposit), is to fabricate shapes by incremental material buildup of thin, planar cross-sectional layers using disposable masks to shape the border of each layer. The ability to spray flat layers is critical for this application. This article describes strategies for optimally spraying onto planar surfaces for applications such as the MD* process.

In the MD* process, a spray torch is manipulated by a robot, and the torch is moved over a target along a trajectory as shown in Fig. 1. The track gap is defined as the distance between two adjacent parallel path segments. The stand-off signifies the distance between the spray torch and the target. The tilt is the angle of the torch axes relative to the target. The goal is to select the trajectory to produce an even coating within the target boundaries.

The distributions of deposited material from conventional thermal spray sources, such as electric arc or plasma torches, typically approximate Gaussian distributions. With a properly selected track gap, Gaussian distributions can be summed to achieve a uniform distribution within the target bounds by overspraying past the mask edges and by moving the torch at a constant speed over the mask opening.[2] The actual distributions will deviate from the ideal Gaussian distribution, however, and will therefore reduce coating uniformity. The factors that contribute to asymmetries, including imperfect mass-flow control, torch geometry, and gas turbulence, cannot always or easily be changed to alter the distribution. Poor alignment of the torch with the substrate also contributes to asymmetry. The distribution, however, can easily be affected by tilting the torch. The stand-off, which also affects the sprayed material distribution, cannot be changed arbitrarily. The physical properties of the coating depend strongly on the temperature and velocity of the impacting droplets,[3-5] which depend on the stand-off.

One approach to smooth asymmetries is to make the track gap small enough to obtain sufficient material overlap between adjacent parallel path segments. For thick coatings (e.g., 0.5 mm to several centimeters), however, the small unevenness of each layer will accumulate so that the surface becomes wavy after hundreds of layers have been deposited. This is unacceptable for applications such as the MD* process. The goal, therefore, is to develop strategies for spraying thick uniform coatings (i.e., 4.0 mm) by modifying the robot trajectories, including tilt angle and track gap. This article describes an approach to optimize robot trajectories to maximize coating flatness based on measured distribution asymmetries.

Keywords: deposition symmetry, dimensional uniformity, electric arc process, manufacturing technology, net-shape manufacture, recursive mask deposition

M.M. Fasching, Institut fur Allgemeine Electrotechnik und Industrielle Elektronik, University of Technology, Vienne, Austria; **F.B. Prinz** and **L.E. Weiss**, Carnegie Mellon University, The Robotics Institute and The Engineering Design Research Center, Pittsburgh, Pennsylvania.

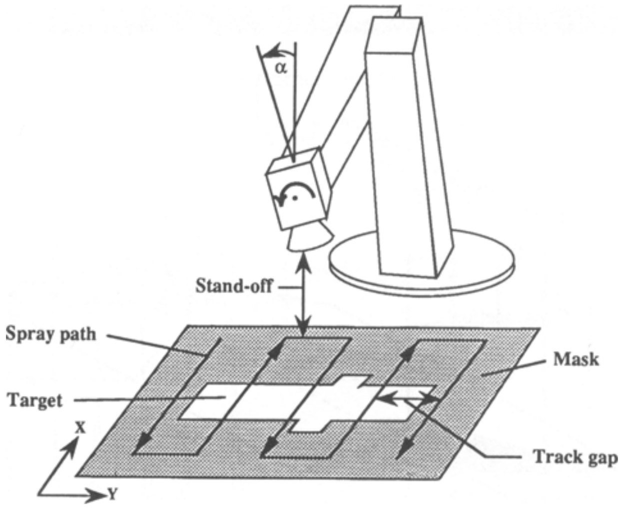

Fig. 1 The spray torch is moved with constant stand-off and constant track gap.

Section 2 describes the measurement procedure and characterization of the actual spray distribution, and Section 3 describes a simple method to symmetrize the material distribution by tilting the spray torch. The resulting distributions are at least symmetric with respect to two perpendicular axes. The equivalence of the distributions with respect to these two axes depends on the properties of the spray torch and cannot be influenced by this method. A small asymmetry of the distribution has a negligible effect on the coating uniformity if the spray path is chosen properly; it is more important to find the optimal track gap, as described in Section 4. In Section 4, the proper selection of robot motion control parameters is also discussed.

2. Measurement of Deposition Symmetry

An accurate model of the deposited material distribution is required to derive the optimal tilt angles and spray path. For the spray trajectory pattern indicated in Fig. 1, it is essential to determine the distributions along both the x and y axes. The measurement of one distribution is produced by first moving the torch along a straight line above and parallel to the x axis, with the geometric axis of the torch approximately normal to the target plane (Fig. 2). To keep the measurement simple and to obtain a reasonable time average of the material buildup, the height of the peak of the deposited material should be allowed to accumulate at least 2.0 mm. The profile of a perpendicular cross section in the middle of the deposited material is then measured.* Depending on the shape of the measured cross section, the spray torch can then be rotated about the x axis by α, as described in Section 3, to compensate for any asymmetry.

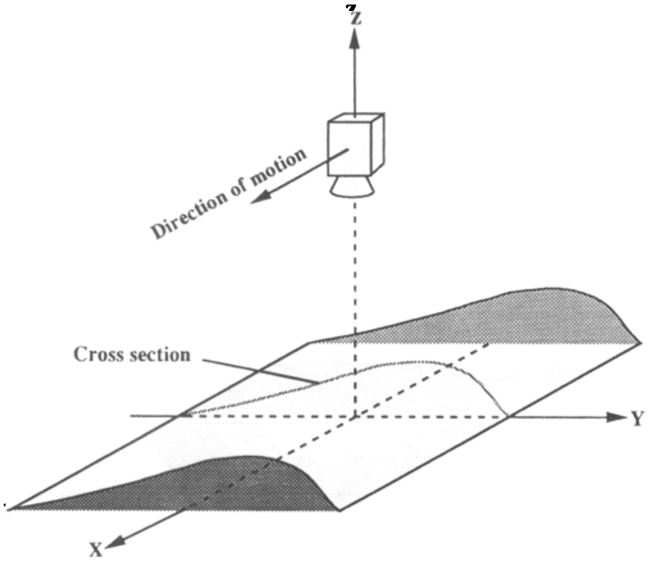

Fig. 2 Measurement of spray distribution.

A typical cross section is shown in Fig. 3. The sample was produced by spraying zinc onto a sand-blasted steel plate with a two-wire electric arc spray system. Figure 4 shows the measured data from that sample distribution. The accuracy of the measurements lies within ±0.005 mm, which is on the order of the magnitude of the sprayed particle sizes. The procedure is repeated in the y direction to determine the second distribution.

Next, a method is required to characterize the symmetry of a two-dimensional data array as in Fig. 4. For this purpose, the statistical variable wryness (γ) is used:[6]

$$\gamma = \frac{\sum_{i=1}^{n} (y_i - \mu)^3 \cdot z_i}{\sigma_y^3}$$

and

$$\sigma_y^2 = \sum_{i=1}^{n} (y_i - \mu)^2 \cdot z_i \quad \mu = \sum_{i=1}^{n} y_i \cdot z_i$$

where y_i and z_i are the coordinates of the i^{th} measured point of the cross section, and σ is the standard deviation. The expected value, μ, of the distribution is that point on the baseline of the cross section which a single particle emanating from the torch hits with the highest probability. The function γ is a very accurate indicator of the tilt of a curve if the data are measured in equidistant steps. The value of γ is zero if the data array is sym-

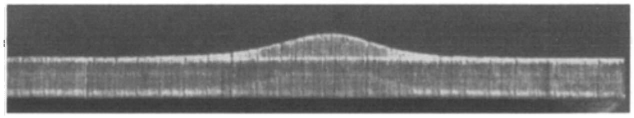

Fig. 3 Characteristic material distribution of zinc sprayed onto sand-blasted steel with a two-wire arc spray system.

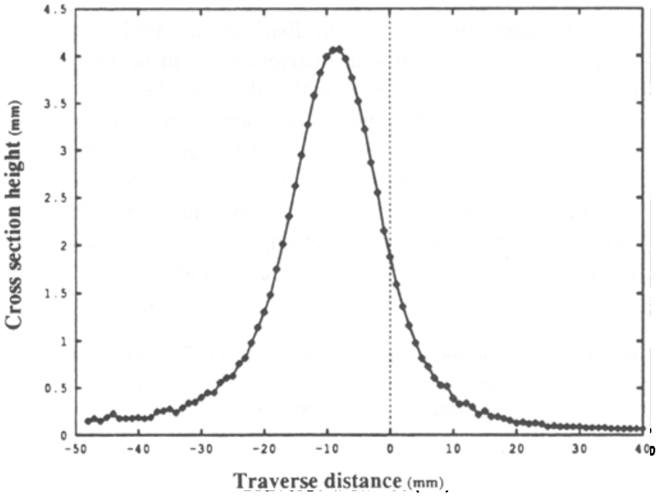

Fig. 4 Measured data array from the cross section formed in Fig. 3.

---

*For this measurement, an electronic contact depth gage that is fixed in the shaft of a milling machine is used. The sample is affixed to the x-y table of the milling machine such that the x and the y spray path align with the x and y axes of the milling machine, respectively. The distribution is then measured in equidistant steps of 1 mm or smaller.

metric with respect to its maximum (μ). It is less than zero if the data curve is tilted to the left; otherwise it is positive.

The following section describes a method for determining the optimal tilt angle about an axis using the corresponding data array and by minimizing the function γ.

3. Torch Tilt Angle Optimization

Tilting the torch changes the material distribution. The redistribution of the measured data array when the torch is tilted by an arbitrary angle α is derived below. For this derivation, the torch is assumed to be fixed while the target plane is tilted. The new data array must then be rotated back to the horizontal plane. Figure 5 shows how a point (A) from the horizontal plane is transformed to a point (A′) on the tilted plane. A mass of particles leaves the torch at an angle ψ. The amount of mass is proportional to the distance, ρ, and approximately the same amount of mass must also precipitate on the tilted plane at the same angle ψ for small rotations. Given the position of the spray torch relative to the target and given the coordinates of the measured data points on the untilted plane, the distance ρ can be calculated. With a given tilt angle, α, the measured data point (A) can be transformed to (A′) on the tilted plane by intersecting the beam emanating from the torch at an angle ψ with the tilted plane.

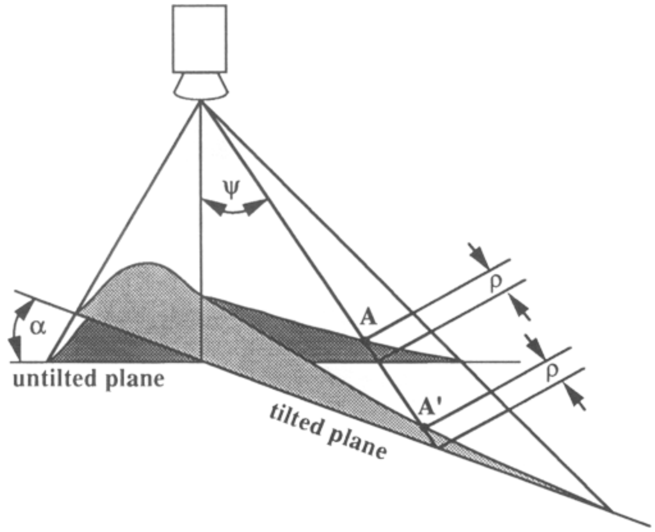

Fig. 5 Transformation of the measured data array.

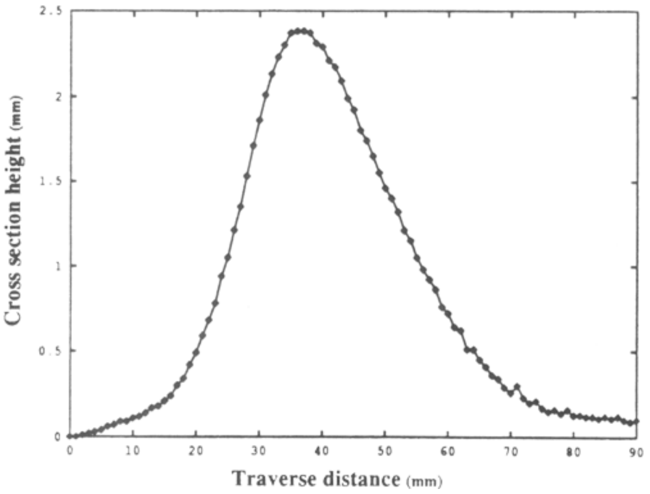

Fig. 6 Measured data array from the cross section formed in Fig. 7.

The data array is then rotated back using the rotation matrix T:

$$\underline{\mathbf{x}} = \mathbf{T} \cdot \underline{\mathbf{x}}'$$

$$\mathrm{T} = \begin{pmatrix} \cos(\alpha) & \sin(\alpha) \\ -\sin(\alpha) & \cos(\alpha) \end{pmatrix}$$

where $\underline{\mathbf{x}}'$ is a point in the tilted coordinate system, and $\underline{\mathbf{x}}$ is a point in the horizontal system. When tilting the torch, it is essential that the torch still points to the same point on the target plane and that the distance between the torch and target is kept constant.

With this transformation and with the previously defined function γ, it is straightforward to find the optimal tilt angle without additional spray experiments. Numerical optimization is used to find the tilt angle that minimizes the function γ. Once the correction angle α for the x axis is found, the procedure is repeated to find the correction angle for the y axis.

The reliability of this method can be tested by measuring and calculating the optimal tilt angle for two distributions; one produced by holding the torch perpendicular to the target plane, the other with an arbitrary angle. The resulting optimal angle between the normal vector of the target plane and the spray torch should be the same for both distributions. For example, Fig. 6 shows the measured data array for the cross section shown in Fig. 7 where the torch was tilted 30°. This data array was used as input for the numerical optimization program. The optimal tilt angle was calculated by the program to be –26.0°, which indicates that the torch must be rotated back to 4.0° to produce a

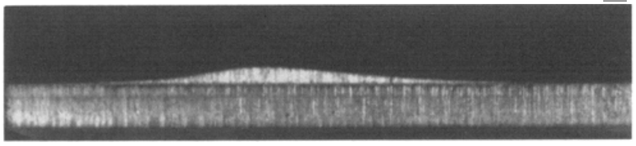

Fig. 7 Zinc sprayed onto steel at an angle of 30°.

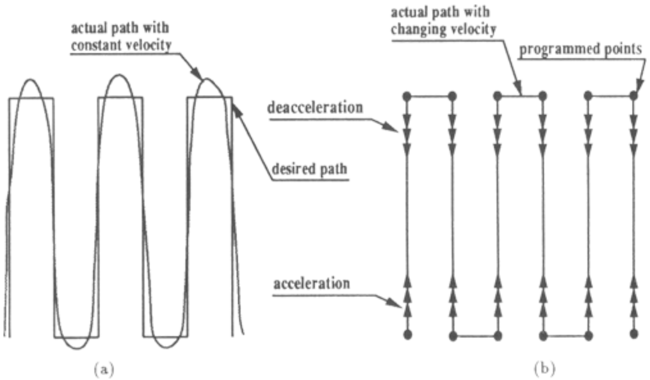

Fig. 8 Movement of the spray torch.

symmetric distribution. This approximately corresponds with the optimal tilt angle of 6.0° calculated for the perpendicular cross section in Fig. 3, where the torch was held perpendicular to the target plane.

This optimization algorithm assumes that the deposition efficiency is independent of the impingement angle of the sprayed particles, that is, the particles impinging normal to the surface stick as well as the particles hitting the target at an acute angle. In practice, the adhesive strength is a function of the spray angle. Its maximum lies between 0 and 30°.[7] The effects due to gas turbulence have also been neglected. In practice, if α is too large (i.e., approximately greater than 30°), then the deposition efficiency decreases and the mechanical properties of the coating also degrade. The typical corrections that are required in the current spray system are on the order of 20° or less; for these cases, the optimization algorithm is valid. The next step is to determine the best spray path based on the optimized distributions.

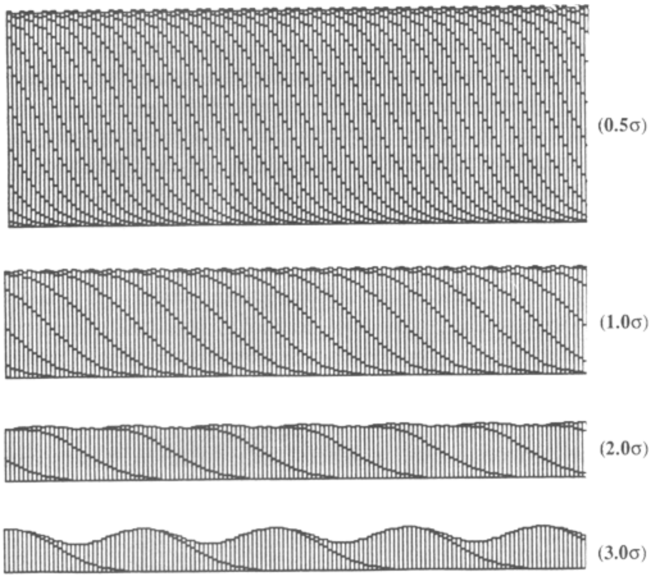

Fig. 9 Simulation of the first layer as a function of the track gap equal to 0.5, 1.0, 2.0, and 3.0 σ.

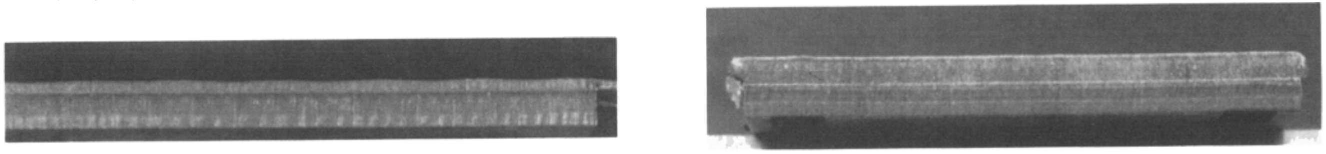

(a) (b)

Fig. 10 Properly aligned torch improves the geometric quality of the surface.

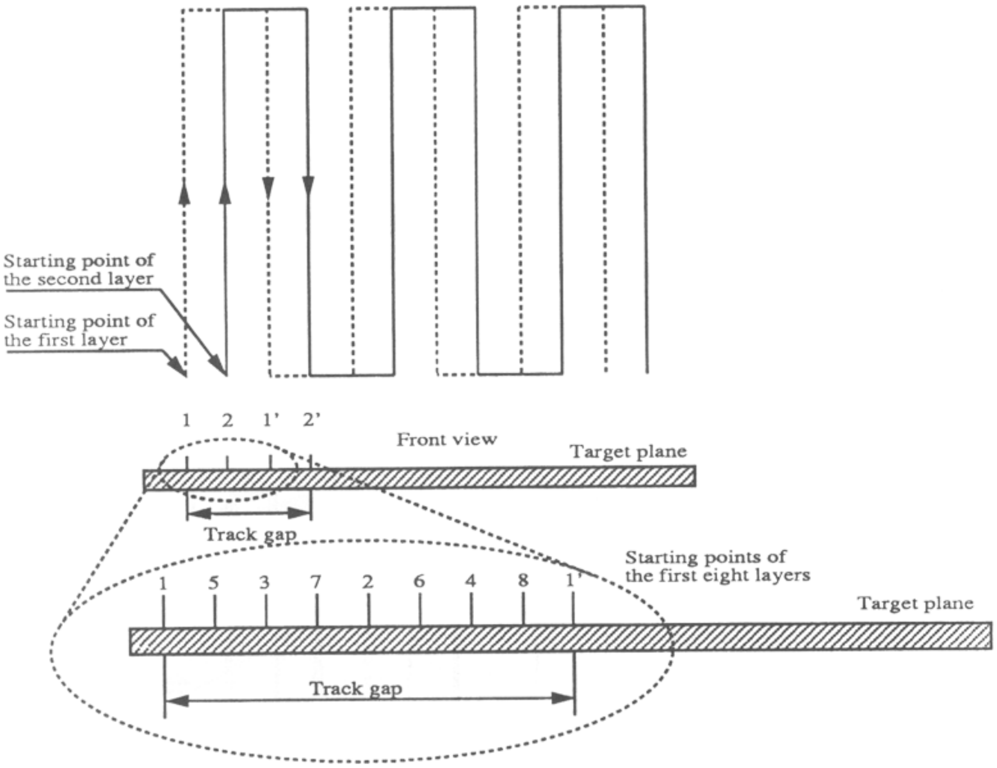

Fig. 11 Shifting the starting points of subsequent layers in a systematic fashion compensates for the small unevenness of each layer.

4. Spray Path Selection

Although the symmetry of the distribution is important, proper selection of the spray path is more critical. As stated earlier, the spray torch is moved by the robot along parallel lines in the x and y directions. The torch should move with a constant velocity along these lines while over the target to maintain a constant deposition rate. The spray path is defined by a set of points along these lines. The robot operating system provides two motion-control alternatives to execute the path. In one mode, movement with constant linear velocity along the path can be specified where the actual path of the torch will deviate from the programmed spray path as a function of the commanded velocity. In the second mode, movement can be programmed exactly from point-to-point using a series of accelerations and decelerations along the path. These two cases are illustrated in Fig. 8. Both types of motion detract from the uniformity of the coating. The decision where to move with constant velocity or to move exactly along the programmed lines depends on the dynamic behavior of the robot system. If point-to-point motion is selected, then the length of the path must be chosen such that the deviations occur outside the working target area; this approach wastes material. Alternatively, the robot can be commanded to move with a low constant velocity, so that the programmed trajectory can be followed more accurately. If the robot moves too slowly, however, the substrate gets too hot and the coating becomes too thick.

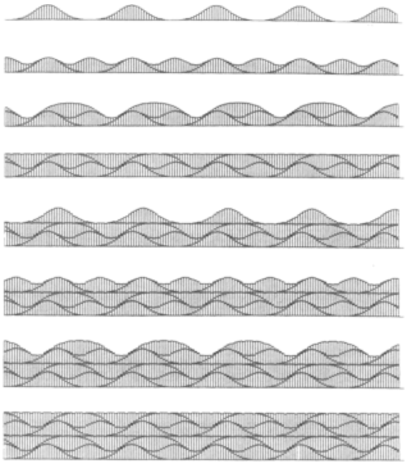

Fig. 12 Evenness improves for an increasing number of layers by choosing the starting points according to Fig. 11.

For electric arc spraying applications, good deposition uniformity can be achieved by specifying constant velocity motion with a track gap distance of one standard deviation (σ) of the corrected distribution. The expected standard deviation is calculated by the simulation program in Section 3. For movement in the x direction, the y spacing between two tracks should be σ_y, and for the movement in y direction, the x spacing should be σ_x. Figure 9 is an example that shows the first layer as a function of the track gap. The simulation was based on a symmetric Gaussian distribution and shows a cross section normal to the sprayed lines. For other symmetric distributions, the "one standard deviation" rule-of-thumb still produces good results. If the track gap becomes larger than one standard deviation, however, the difference in the evenness between Gaussian and non-Gaussian coatings can be significant.

Figure 10 illustrates how the geometric quality of the surface improves with tilt and path optimization. The coating in the first example (Fig. 10a) was sprayed with the torch held at a right angle to the target plane. The track gap was 1.2 standard deviations. This suboptimal trajectory produced a wavy, uneven coating. In the second example (Fig. 10b), the material distribution was symmetrized using the aforementioned tilt procedures, and the track gap was set to 1.0 standard deviations. There is a clear improvement in coating uniformity. The mean thickness of the coating is 3.93 mm, which is approximately twice as thick as the first sample. The measured standard deviation from the mean thickness ranges from 20.0 to 30.0 μm.

Theoretically, the best coating uniformity can be produced by allowing the track gap to approach zero. In this case, the center of the torch moves over every point of the target plane; thus the coating would be perfectly even. This is valid for any shaped distribution. Although smaller track gaps produce more uniform coatings, the coatings become thicker and the substrate becomes hotter. In cases where thin and even coatings are required, the torch speed must therefore be increased as the track gap is reduced. This is limited by the dynamic properties of the robot.

Thick even coatings can also be achieved by systematically depositing and accumulating thin uneven layers. For this approach, the first layer is sprayed as usual with a track gap of one standard deviation. The starting points of subsequent layers are then selected to lie between the first two lines of the first trajectory. Figure 11 illustrates how the starting points of the subsequent eight layers, for example, would be chosen. The starting points are distributed between the first two lines of the first layer so that the starting points of ($2^n - 1$) layers will fill the track gap

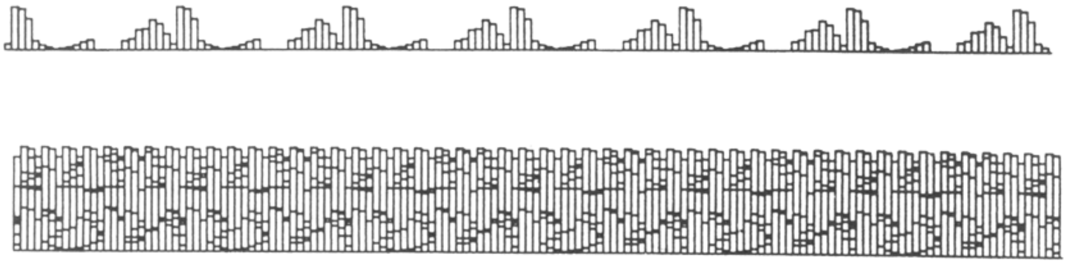

Fig. 13 Simulation of the first and eighth layer of a coating using different starting points of each layer according to Fig. 11, sprayed with an asymmetric distribution.

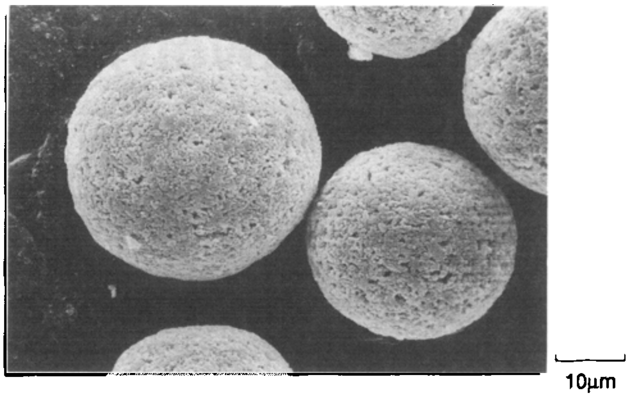

Fig. 1 Powder morphology of $2CaO{\cdot}SiO_2$-$25CaO{\cdot}ZrO_2$.

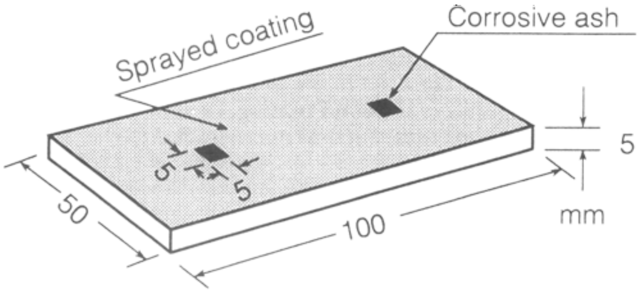

a) For hot corrosion test

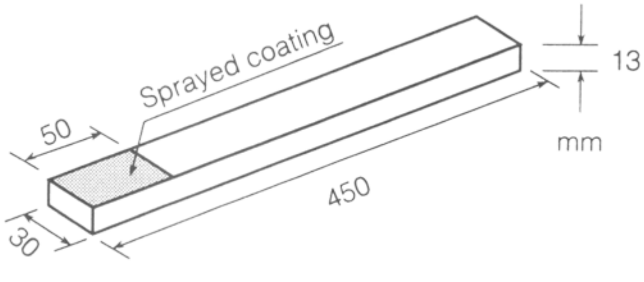

b) For thermal cycle test

Fig. 2 Schematic of thermal barrier coating specimens.

ceramic topcoat in a double layer. The composition of coating materials and the spraying conditions are shown in Table 1. The Ni-21Cr-10Al-0.8Y (wt%) alloy was plasma sprayed to a thickness of 100 µm before the spraying of ceramic coatings. C_2S-CZ ceramics with different contents of $CaO{\cdot}ZrO_2$ (CZ) were sprayed to a thickness of 300 µm. The ceramic powders were prepared by the spray drying method. The powder morphology C_2S-25 CZ (wt%) (C_2S-25CZ) observed through a scanning electron microscope (SEM) is shown in Fig. 1. To provide a reference, the commercially available $8Y_2O_3$-ZrO_2 (wt%) (8YZ) was also plasma sprayed on the same specimen. Figure 2 shows schematically the shape and dimensions of the thermal barrier coating specimens.

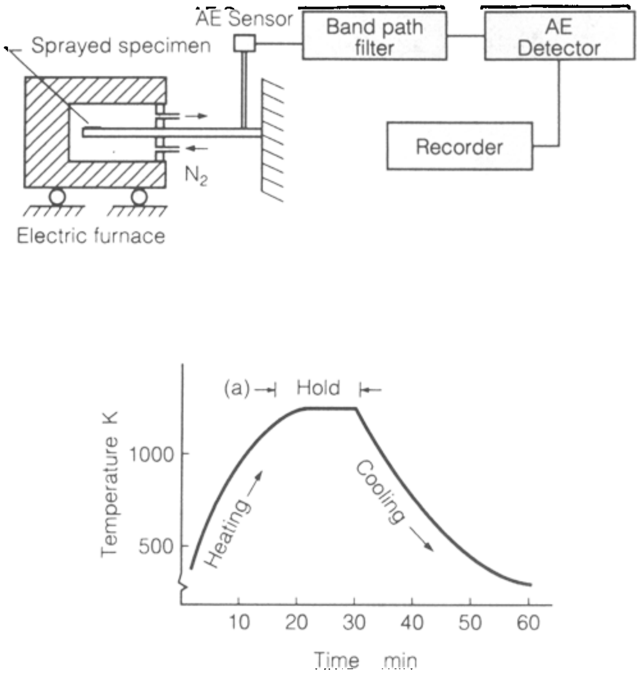

Fig. 3 Schematic of acoustic emission monitoring thermal cycle test for thermal barrier coatings and the thermal cycle used in the experiment.

2.2 *Thermal Shock Test*

As shown in Fig. 2(a), a part of the specimen (area of 50 by 30 mm) was plasma sprayed, while the acoustic emission (AE) sensor was attached to the uncoated part of the same specimen. The coated part of the specimen was then repeatedly heated in an electric furnace at 1273 K, for 15 min and cooled in air. Figure 3 shows schematically the test apparatus and thermal cycle used in the thermal shock test. During the test, the specimen was fixed and the electric furnace, which was maintained at 1273 K, was moved backwards and forwards to heat and cool the specimen. The acoustic emission signal from the specimen was transmitted to the recorder through the band pass filter.

2.3 *Hot Corrosion Test*

The center part of the specimen shown in Fig. 2(b) was covered with 10 mg/cm^2 of corrosive ash. The smearing area was limited to 5 by 5 mm. The composition of the corrosive ash was $85V_2O_5$-$15Na_2SO_4$ (wt%). The specimen smeared with ashes was kept in an electric furnace at 1273 K for 3 h.[13] After hot corrosion testing, the corrosion resistance of the specimen was evaluated by observing the external appearance and examining the structure of the coatings by X-ray diffraction analysis and electron probe microanalysis (EPMA).

3. Experimental Results

3.1 *Microstructure of the Coatings*

The SEM micrographs of the plasma sprayed coatings are shown in Fig. 4. Many microcracks are observed in the C_2S-CZ

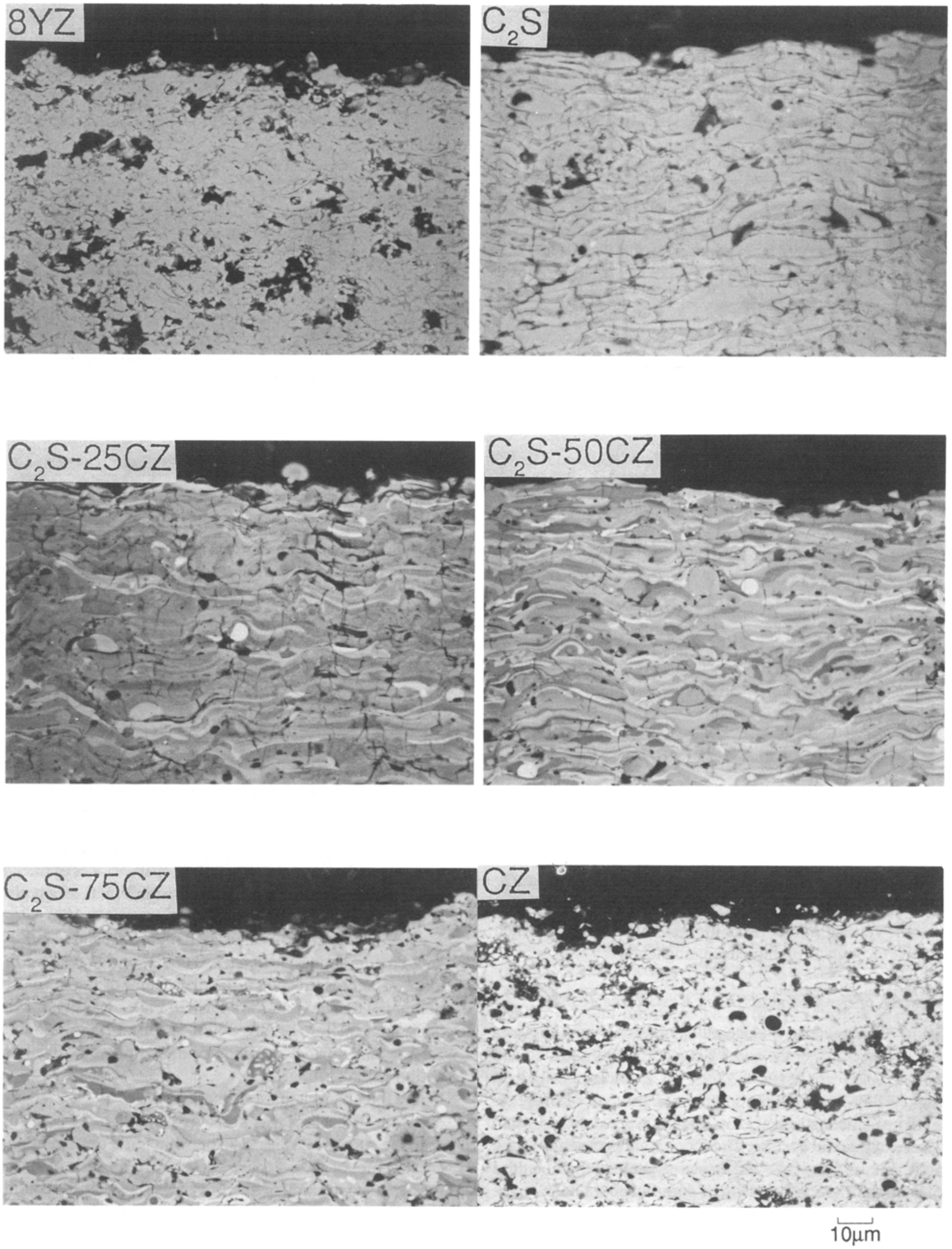

Fig. 4 Microstructure of the cross section of various coatings used in the study.

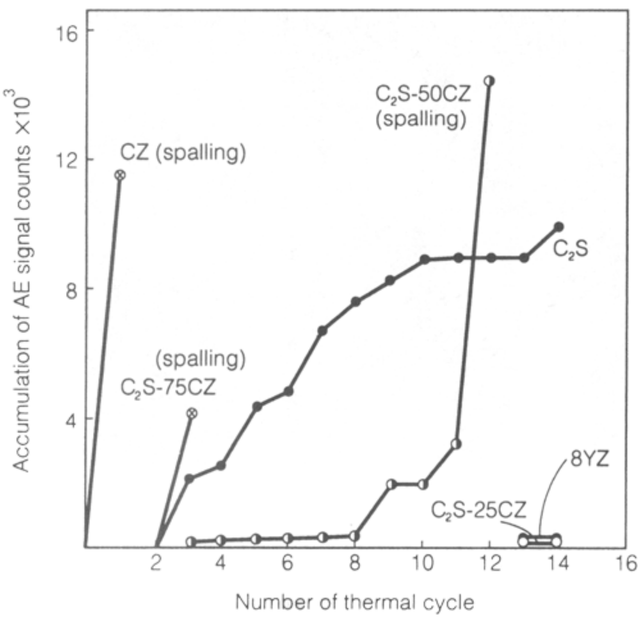

Fig. 5 Accumulation of acoustic emission signal counts of coatings during the thermal cycle test.

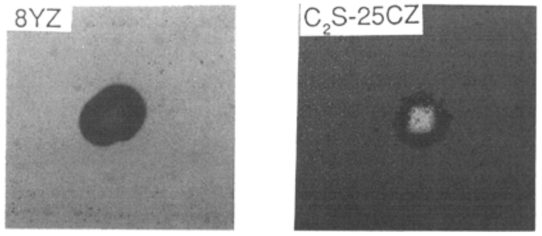

Fig. 6 External appearance of $8Y_2O_3{\cdot}ZrO_2$ and $2CaO{\cdot}SiO_2$-$25CaO{\cdot}ZrO_2$ coatings after hot corrosion testing with $85V_2O_5{\cdot}15Na_2SO_4$ at 1273 K for 3 h.

coatings. In particular, the C_2S-25CZ coating has many relatively short vertical microcracks in individual particles, which do not pass through the complete coating layer.

3.2 *Results of the Thermal Shock Resistance Test*

Figure 5 summarizes the acoustic emission count numbers detected when the C_2S-CZ and 8YZ coatings were heated and cooled.[14] In the case of CZ and C_2S-75CZ coatings, which do not contain SiO_2 and contain only a small amount of SiO_2, respectively, the acoustic emission signals were detected at an early stage of thermal cycling. The CZ coating peeled off during the first cycle, and the C_2S-75CZ coating peeled off at the third cycle. With the C_2S coating, which does not contain ZrO_2, the acoustic emission signals were detected from the third cycle, and then gradually increased as thermal cycling continued. No spallation of the coatings, however, occurred.

Conversely, few acoustic emission signals were detected up to the 14th thermal cycle in the case of the C_2S-25CZ coating, which exhibited numerous vertical microcracks, and no visible damage was observed on the surface. Consequently, it has been concluded that the C_2S-25CZ coating equaled the 8YZ coating in thermal shock resistance.

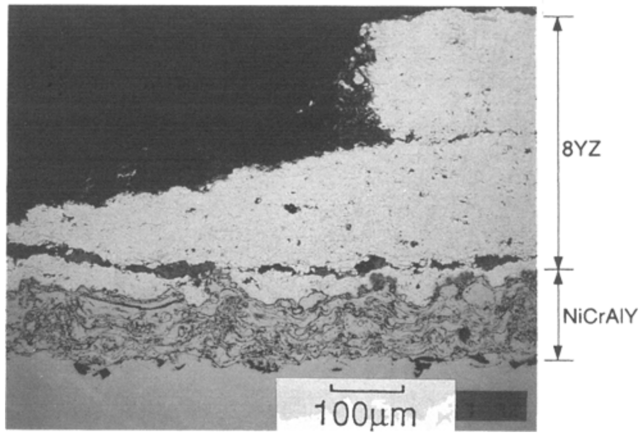

Fig. 7 SEM photograph of cross section of $8Y_2O_3{\cdot}ZrO_2$ coating corroded by $85V_2O_5{\cdot}15Na_2SO_4$ at 1273 K for 3 h.

Table 2 Summary of hot corrosion testing with corrosive ashes at 1273 K for 3 h

Coatings	Results
$8Y_2O_3{\cdot}ZrO_2$	Cracks and minor spalling
C_2S	Attacked and minor cracks
C_2S-25CZ	Color change
C_2S-50CZ	Attacked and minor cracks
C_2S-75CZ	Cracks and spalling
CZ	Cracks and spalling

3.3 *Results of Hot Corrosion Testing*

Results of visual inspection (with the unaided eye) of the coating surface after the specimen was exposed at 1273 K for 3 h is summarized in Table 2. The external surfaces of the 8YZ[15] and C_2S-25CZ coatings are illustrated in Fig. 6, as a typical example of hot corrosion damage.

The distinct color changes to dark brown and peeling of the 8YZ coating suggested that it had undergone attack by corrosive ashes. The cross-sectional microstructure of the corroded portion of the 8YZ coatings is shown in Fig. 7. It is evident that the horizontal fracture occurred in the topcoat and at the interface between the topcoat and undercoat, as well as a partial delamination of the coating.

On the other hand, in the case of the C_2S-25CZ coating, no evidence of peeling was observed, although the area smeared with the corrosive ashes became white. The cross-sectional microstructure of the corroded part shown in Fig. 8 indicates that the chemical reaction of the corrosive ashes with the coating was limited to the layer near the coating surface. The other parts of the coating, including the interface between the ceramic coating and the undercoat layer, were unchanged. Further systematic investigations of C_2S-CZ coatings have confirmed that only a limited amount of the 10~30CZ component exhibited many effective vertical microcracks. These cracks improved thermal

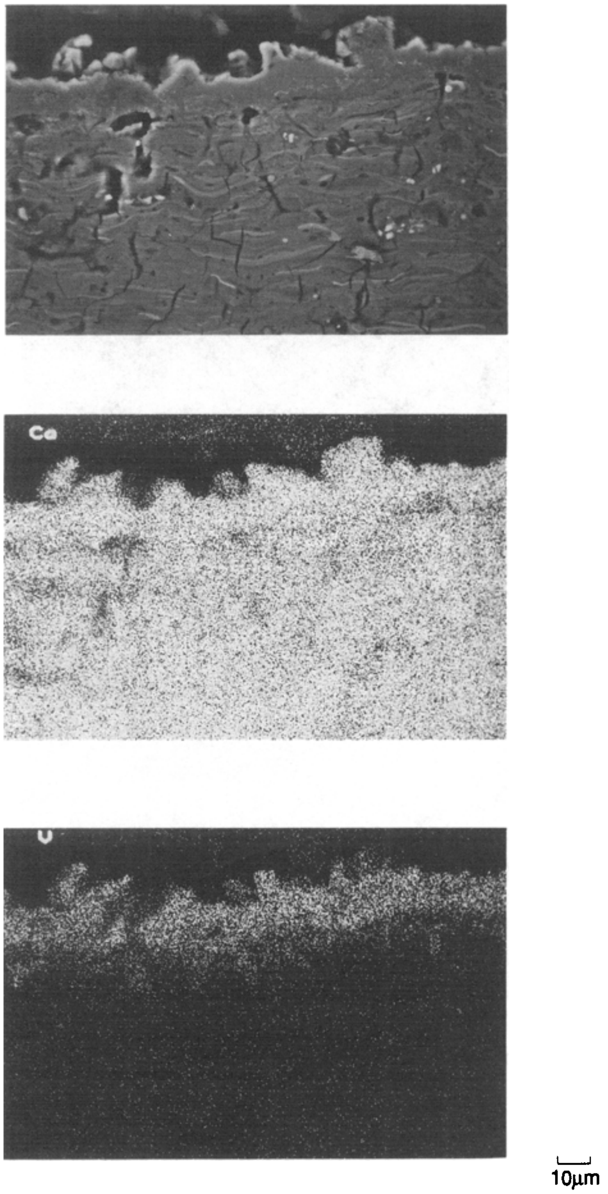

Fig. 8 SEM photograph and X-ray images of a cross section of the $2CaO{\cdot}SiO_2$-$25CaO{\cdot}ZrO_2$ coating corroded by $85V_2O_5{\cdot}15Na_2SO_4$ at 1273 K for 3 h.

shock resistance, and the samples demonstrated high hot corrosion resistance.

4. Discussion

4.1 *Microstructure of $2CaO{\cdot}SiO_2$-$CaO{\cdot}ZrO_2$ Coatings and Thermal Shock Resistance*

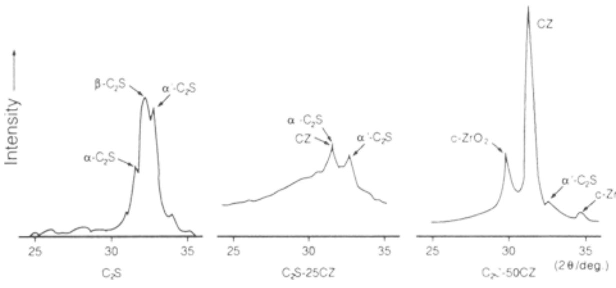

Fig. 9 X-ray diffraction pattern of sprayed coatings.

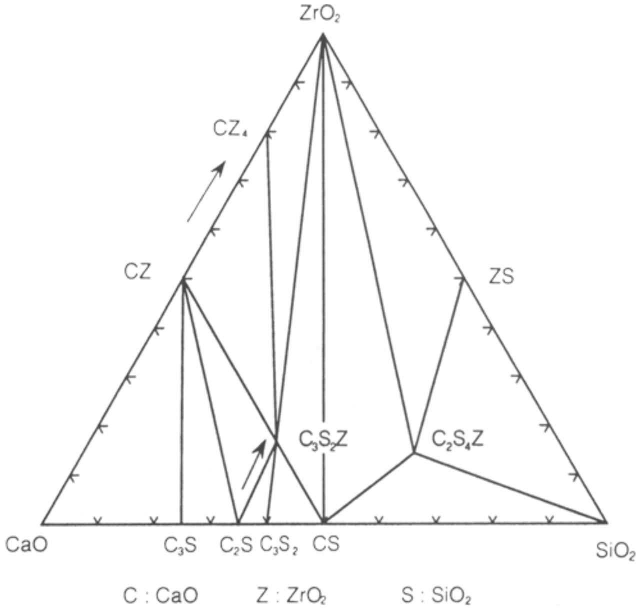

Fig. 10 Phase diagram of the ZrO_2-CaO-SiO_2 system.

The excellent thermal shock resistance of the C_2S-25CZ coating may be attributed to thermal stress release by the vertical microcracks. The X-ray diffraction pattern of the sprayed coatings is shown in Fig. 9. In the C_2S-CZ system, α, α', and β-C_2S phases were identified. In particular, the C_2S-25CZ coating exhibited a broad diffraction pattern, indicating that it had an amorphous phase. The amorphous phase is the result of a shift in chemical composition toward the three-component system, C_2S-CZ-C_3S_2Z, in the phase diagram[16] shown in Fig. 10 due to the sublimation of CaO at 3123 K.[17] This is the most unstable component in the C_2S-CZ system in a plasma environment. The sublimation of CaO during the plasma spraying process was previously observed by Gitzhofer.[18] The behavior of CaO, which sublimates at a temperature near its melting point (3025 K), and the presence of SiO_2, which is likely to form glassy material, may facilitate the creation of the amorphous phase. The C_2S-CZ-C_3S_2Z three-component system may decompose into cubic ZrO_2 (CZ_4) + C_2S at a lower temperature (1908 K)[19] and produce the liquid phase. The ceramic particles, which were liquified in the plasma environment, impact and adhere to the deposited ceramic or metal particles. At the same time, the flattened particles, which are transformed into a brittle solid phase from a liquid phase by means of quenching, induce tensile stress on the outside of the particles. Subsequently, it is expected that the tensile stress gave rise to microcracks within the single flattened ceramic particle. In addition, few horizontal microcracks exist on the grain boundary, because the adhesion between each particle results in strong bonding. As discussed above, the C_2S-25CZ coating demon-

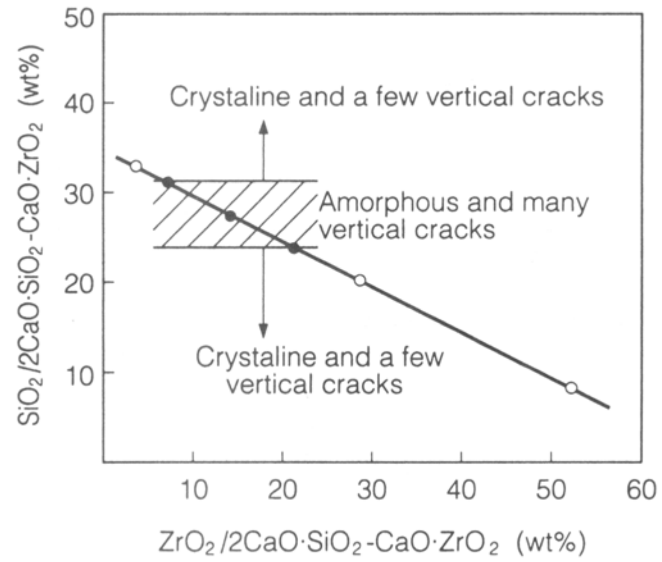

Fig. 11 Relationship between crystallinity of $2CaO \cdot SiO_2$-$CaO \cdot ZrO_2$ coatings and vertical microcracks.

Table 3 X-ray analysis of coatings corroded with $85V_2O_5 \cdot 15Na_2SO_4$ at 1273 K for 3 h

Coatings	Corrosion products
$8Y_2O_3 \cdot ZrO_2$	YVO_4, $Y_8V_2O_{17}$
C_2S-25CZ	$Ca_2V_2O_7$, CaV_2O_6, $CaSO_4$, SiO_2

strated excellent thermal shock resistance because the vertical microcracks prevent the occurrence of horizontal cracks and thus absorb the stress of thermal shock.

On the other hand, it has been confirmed that only a limited amount of the amorphous phase appeared in the 10 to 30% CZ in the C_2S-CZ coatings. Figure 11 summarizes the degree of crystallization obtained by X-ray diffraction analysis and vertical microcracks of the cross section on the C_2S-CZ coatings relative to SiO_2 content and ZrO_2 content in the C_2S-CZ powder materials, respectively. The results have demonstrated that the C_2S-CZ coatings, which consist of 25 to 30% SiO_2, 7 to 20% ZrO_2, and the balance CaO, exhibited amorphous phase and many vertical microcracks, thus improving thermal shock resistance.

4.2 *Hot Corrosion Resistance*

Figure 12 shows the morphology of the surface of the as-sprayed 8YZ and C_2S-25CZ coatings. It can be expected that the molten corrosive ashes easily penetrate the coating through the microcracks and voids that were formed when the molten ceramic particles in the plasma flame were quenched and solidified. Although the voids and microcracks in the sprayed coating are beneficial in that they increase the thermal insulation characteristics due to the reduction of the thermal conductivity and the release of the thermal stress, they, nonetheless, reduce corrosion resistance by allowing the penetration of corrosive liquid or gas into the coating. X-ray diffractometry was applied to the corroded parts of the coating to investigate the chemical reaction

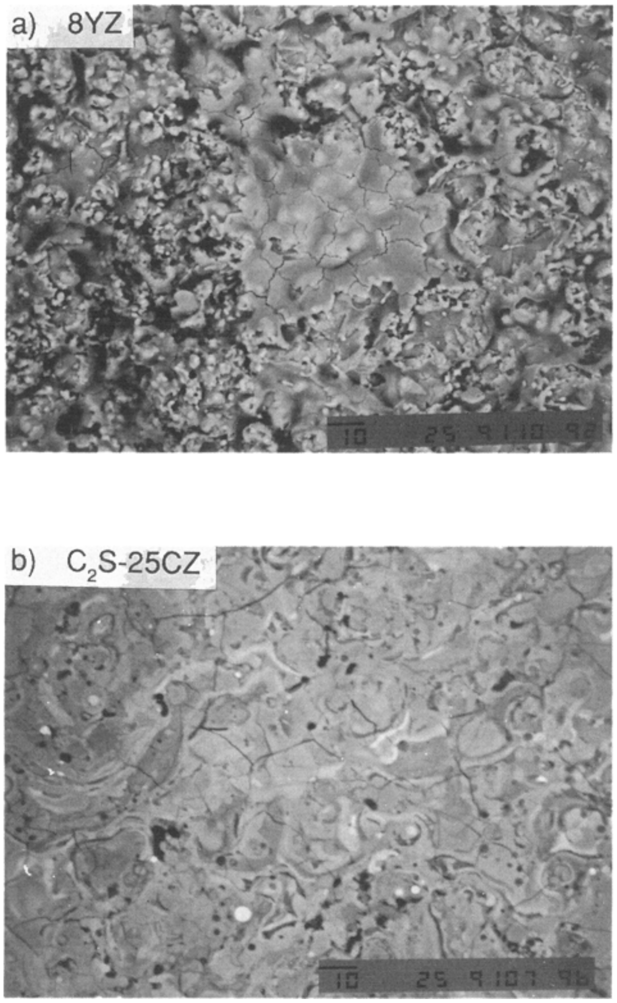

Fig. 12 Surface morphology of as-sprayed coatings.

between the ceramic coating and the corrosive ashes. Table 3 summarizes the results. It was found that the Y_2O_3 component in the 8YZ coating reacted with V_2O_5 (melting point = 891 K) to form YVO_4 and $Y_8V_2O_{17}$,[20] and no sulfur compound was formed. In the case of the C_2S-25CZ coating, reaction products such as $Ca_2V_2O_7$, CaV_2O_6, and $CaSO_4$ were identified.

The spalling of 8YZ coatings was assumed to be caused by the phase transformation of ZrO_2 between the tetragonal and monoclinic phases due to the consumption of Y_2O_3 through a chemical reaction with V_2O_5.[21] In the C_2S-25CZ coating, on the other hand, the coexisting amorphous phase (SiO_2-rich phase) suppresses an excess consumption of the CaO component in the coating, and a stable compound such as $Ca_2V_2O_7$ (melting point = 1288 K) was formed by a reaction between CaO and V_2O_5. The reacted layer acts as a barrier against the molten corrosive ashes and prevents the corrosion ashes from penetrating into the coatings. As a result, C_2S-25CZ coatings are considered to exhibit excellent corrosion resistance.

Additionally, in this experiment, no penetration of the corrosive component into the vertical microcracks in the C_2S-25CZ coating was observed.

5. Conclusions

Plasma-sprayed C_2S-CZ coatings were developed to improve the high-temperature performance of gas turbines. The results were as follows. Many vertical microcracks were formed in as-sprayed C_2S-CZ coatings containing 10 to 30% CZ. Because of the vertical microcracks, the coatings exhibited an excellent spallation resistance during repeated thermal cycling tests. The coatings with vertical microcracks consisted of α, α'-C_2S, CZ and amorphous phases. The microcracks were produced in the course of the rapid cooling of flattened particles after solidification of molten particles. The molten particles result from the C_2S-CZ-C_3S_2Z three-component system due to the sublimation of CaO during the thermal spraying process.

Although the CaO component in the ceramics is partially consumed by a chemical reaction with vanadium compounds, the area where the reaction takes place is limited to the space where the corrosive ashes make contact with the coating. The coating exhibited excellent hot corrosion resistance and is, therefore, a promising material for thermal barrier coatings.

Acknowledgment

On achieving the investigation by the thermal cycling acoustic emission inspection apparatus, as well as coating development, we would like to thank Mr. Junichi Ikeda, Mr. Shinichi Tamura, and Mr. Hatsuo Taira of FCDD of Nippon Steel Corporation.

References

1. R. Tanaka, "The Trend of Heat Resistant Alloy Materials," Proc. Symp. Jpn. Inst. Metals, Nov 1981, p 209-210 (in Japanese)
2. A.S. Grot and J.K. Martyn, Behavior of Plasma-Sprayed Ceramic Thermal-Barrier Coatings for Gas Turbine Applications, *Ceram. Bull.*, Vol 60(No. 8), 1981, p 807-811
3. N. Iwamoto, Development on Coatings for Gas Turbine, *J. Iron Steel Inst. Jpn.*, Vol 73(No. 16), 1987, p 33-42 (in Japanese)
4. P.E. Hodge, S. Stecura, M.A. Gedwill, I. Zaplatynsky, and S.R. Levine, "Thermal Barrier Coatings: Burner Rig Hot Corrosion Test Results," NASA TM-79005, NASA Lewis Research Center, Cleveland, Oct 1978
5. J.D. Reardon and M.R. Dorfman, Advanced Thermal Barrier Coating System, *J. Mater. Energy Syst.*, Vol 8(No. 4), Mar 1987, p 414-419
6. S. Stecura, New ZrO_2-Yb_2O_3 Plasma-Sprayed Coating for Thermal Barrier Applications, *Thin Solid Films*, Vol 150(No. 1), 1987, p 15-40
7. D.S. Duvall and D.L. Ruckle, Ceramic Thermal Barrier Coatings for Turbine Engine Components, ASME Paper 82-GT-322, p 1-9
8. Y. Kojima, S. Ogawa, and N. Asahi, Japan Patent Publication No. 58-87273 (in Japanese)
9. T. Degawa, Japan Patent Publication No. 59-140377 (in Japanese)
10. K. Nezaki, Y. Nakanishi, R. Katsutani, N. Morishige, T. Irisawa, and T. Ota, "Effect of Laser Cracking Method, Improvement of Failure Characteristics of Thermal Barrier Coating," Rept. 1, *Proc. Jpn. Welding Soc.*, Vol 47, Oct 1990, p 184-185 (in Japanese)
11. B.A. Nagaraj, A.F. Maricocchi, E. Whitney, and D.J. Wortman, "Corrosion Resistance of Plasma Sprayed and Laser Glazed Ceramic Coatings," Conference on Plasma and Laser Processing of Materials, New Orleans, 1991, p 375-380
12. J.W. Vogan, L. Hsu, and A.R. Stetson, Thermal Barrier Coatings for Thermal Insulation and Corrosion Resistance in Industrial Gas Turbine Engines, *Thin Solid Films*, Vol 84, 1981, p 75-87
13. H. Nakahira, Y. Harada, N. Mifune, and T. Doi, Hot Corrosion Behavior of Plasma Sprayed Thermal Barrier Coatings and Acoustic Emission Response to Corrosion Monitoring, *J. Soc. Mater. Sci. Jpn.*, Vol 40(No. 455), 1991, p 989-995 (in Japanese)
14. H. Taira, H. Imaoka, K. Kanematsu, S. Tamura, T. Yogoro, and N. Mifune, "Thermal Shock Resistance of Plasma Sprayed $2CaO{\cdot}SiO_2$-$CaO{\cdot}ZrO_2$ Coatings," *Proc. Ceramic Soc. Jpn*, Vol 3E32, 1991, p 577 (in Japanese)
15. T. Doi, H. Nakahira, Y. Harada, and N. Mifune, Hot Corrosion Resistance of $8Y_2O_3{\cdot}ZrO_2$/NiCrAlY Graded Thermal Barrier Coating Formed by Plasma Spraying Process, *J. High Temp. Soc.*, Vol 17, Suppl, 1991, p 406-414 (in Japanese)
16. T. Uetsuki, K. Tanaka, M. Maekawa, T. Ota, N. Tamaki, and Y. Nakazawa, The Compatibility Relationships in the System $ZrO_2{\cdot}CaO{\cdot}SiO_2$ at 1400 to 1500 °C, *Yogyo-Kyokai-shi*, Vol 93(No. 8), 1985, p 418-425 (in Japanese)
17. *Dictionary of Physics and Chemistry*, B. Tamamushi, Ed., Iwanami, Tokyo, Japan, 1979 (in Japanese)
18. F. Gitzhofer, D. Lombord, A.M. Vardelle, C. Martin, and P. Fauchais, "Thermophysical Properties of Zirconia Coatings Stabilized with Calcia or Yttria: Influence of Spraying Parameters and Heat Treatment," Proc. 11th Int. Thermal Spray Conf., Montreal, Canada, 1986, p 269-275
19. T. Uetsuki, K. Tanaka, and Y. Nakazawa, The Fundamental Study on the Application of the System $ZrO_2{\cdot}SiO_2{\cdot}CaO$ for the High Temperature Material, *Rept. Asahi Glass Found. Ind. Technol.*, Vol 45, 1984, Asahi Glass Co., Ltd., Tokyo, Japan (in Japanese)
20. D.W. McKee and P.A. Siemers, Resistance of Thermal Barrier Ceramic Coatings to Hot Salt Corrosion, *Thin Solid Films*, Vol 73, 1980, p 439-445
21. P. Vincenzini, Zirconia Thermal Barrier Coatings for Engine Applications, *Ind. Ceram.*, Vol 10(No. 3), 1990, p 113-126